# Structural performance of composite WikiHouse beams from CNC-cut timber panels

# Structural performance of composite WikiHouse beams from CNC-cut timber panels

Gabriele Granello[1], Thomas Reynolds[2] and Clayton Prest [3]

**Accepted for publication in Engineering Structures**

## ABSTRACT

Computer-numerical-control (CNC) fabrication of interlocking-plate timber structures is a promising form of construction for housing with the potential to be socially, economically and environmentally sustainable. The primary mechanisms of load transfer in these structures rely on direct contact and friction between interlocking elements, without the nails and screws used in conventional timber structures. The development of these connections is relatively new, and therefore the application of interlocking plates structural systems in real projects is so far limited. In this study, the WikiHouse interlocking-plate timber structural system for digitally fabricated houses is presented from a design and fabrication point of view. The main structural elements of the system, the beams and columns, are hollow section members fabricated using computer-numerical-control (CNC) cut plywood panels. In the first part of the paper, the concept of Wikihouse and its fabrication process are presented. Then, the performance of the structural beams is investigated by means of experimental testing on full scale 5 m specimens. Finally, an analytical model to calculate the beam capacity and displacements is derived based on elastic beam bending and joint flexibility. Results show that the specimens failed in a ductile manner. Furthermore, it was found that the joints between the panels introduce extra flexibility to element, and that rigid-body rotations occurring in the joints within the span make a substantial contribution to the overall deflection.

**Keywords:** WikiHouse, Digital fabrication, timber, plywood, all-timber joints; carpentry

## INTRODUCTION

Novel off-site construction methods have been subject to intensive research in recent years, with the goal of increasing the efficiency of the construction industry (Pan

[1]Research Associate, Institute for Infrastructure and Environment, School of Engineering, University of Edinburgh. e-mail: ggranell@ed.ac.uk

[2]Chancellor's Fellow, Institute for Infrastructure and Environment, School of Engineering, University of Edinburgh. e-mail: T.Reynolds@ed.ac.uk

[3]Research and Development Lead, Open System Lab. e-mail: clayton@opensystemslab.io

et al. 2008; Pan and Sidwell 2011; Arif et al. 2012; Boyd et al. 2013; Hosseini et al. 2018; Hairstans and Smith 2018; Duncheva and Bradley 2019).

Off-site construction consists of transferring a portion of the construction process from the building site to a more controlled factory or workshop environment (Hairstans 2017). This potentially provides several benefits, such as improved quality of the final product, waste reduction, and reduced assembly time on site (Goodier and Gibb 2005; Krug and Miles 2013).


FIG. 1: Wikihouse buildings (courtesy of Open Systems Lab): a) South Yorkshire Housing Association, UK; b) Wikihouse Pavillon, Netherlands c), d) A-barn, Scotland; e), f), g) Farmhouse Warwickshire, UK. Further details at https://www.wikihouse.cc/Projects.

Some degree of off-site construction is common in contemporary timber construction: structural elements are often fabricated in the factory and later assembled on site (Mayo 2015). A further benefit of timber is that its high workability is well suited for *digital fabrication* (Beorkrem 2017), i.e., the process of manufacturing that involves computer-numerical-control (CNC) machining. Where CNC machining is used, the design is digitised as a three-dimensional model of the part to be fabricated. This leads to the potential for further gains in efficiency through the integration of design and manufacturing within the same workflow (Nguyen et al. 2019).

Švajlenka and Kozlovská (2020) show that off-site fabricated timber building systems have the potential to be environmentally, economically and socially sustainable. Therefore, significant effort has been placed in the last years in proposing innovative manufacturing processes of timber structures.

For example, Magna et al. (2013) developed a biomimetic design methodology based on the analysis of the Echinoids. The authors proposed a framework for designing and fabricating timber shell structures, which integrates finite element modelling with fabrication constraints. Gattas and You (2016) studied the concept and application of folded sandwich structures, building complex surfaces using rules for combination of simple shapes. In their study, the authors showed the design to fabrication process: from 1) original surface to 2) pattern conversion to 3) manufacture rationalization to 3) connection superposition. Willmann et al. (2016) presented an overview of robotic timber construction technologies. Among the various projects, it was shown the development of a 6 degrees of freedom large-scale setup, which can handle timber components of a length between 0.5 m to 10 m and can manufacture building elements up to 48 m length.

From a digital fabrication point of view, the most commonly adopted strategy for timber consists of developing integral timber to timber connections, also known as integral mechanical attachments (Sass 2007). Such connections allow the assembly of structural elements without (or with few) additional fixings, with the benefit of reducing construction time (Robeller 2015).

The structural performance of integral mechanical attachments was experimentally investigated by Rad et al. (2019). The study investigated the effect of timber species, angles between the panels, and fiber-orientation in the structural performance of the connection. Among other findings, the authors showed that the ductility of the connection is largely dependant on the fibre-orientation with respect to the load direction.

Numerical models, such as for example the simplified springs models (Nguyen and Weinand 2018) or detailed finite element models (Stitic et al. 2019), were also used in literature to calculate the behaviour of such joints. This facilitated the use of integral mechanical attachments in real projects.

There have been various practical implementations of these systems, such as for example the "instant House" (Sass and Botha 2006), the "Landesgartenschau Exhibition Hall" (Li and Knippers 2015) and the "Théâtre Vidy Lausanne" (Robeller et al. 2017). These structures are however unique and designed ad hoc. And to date, there has not yet been a widespread application that could take advantage of the potential efficiencies in design and construction for housing and community developments.

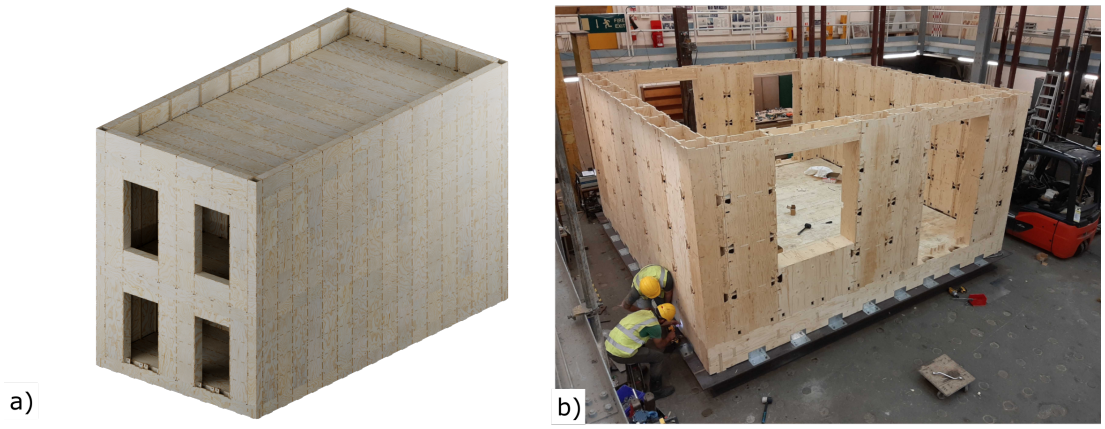


FIG. 2: Wikihouse Skylark a) architectural render , b) building module under construction in the laboratory.

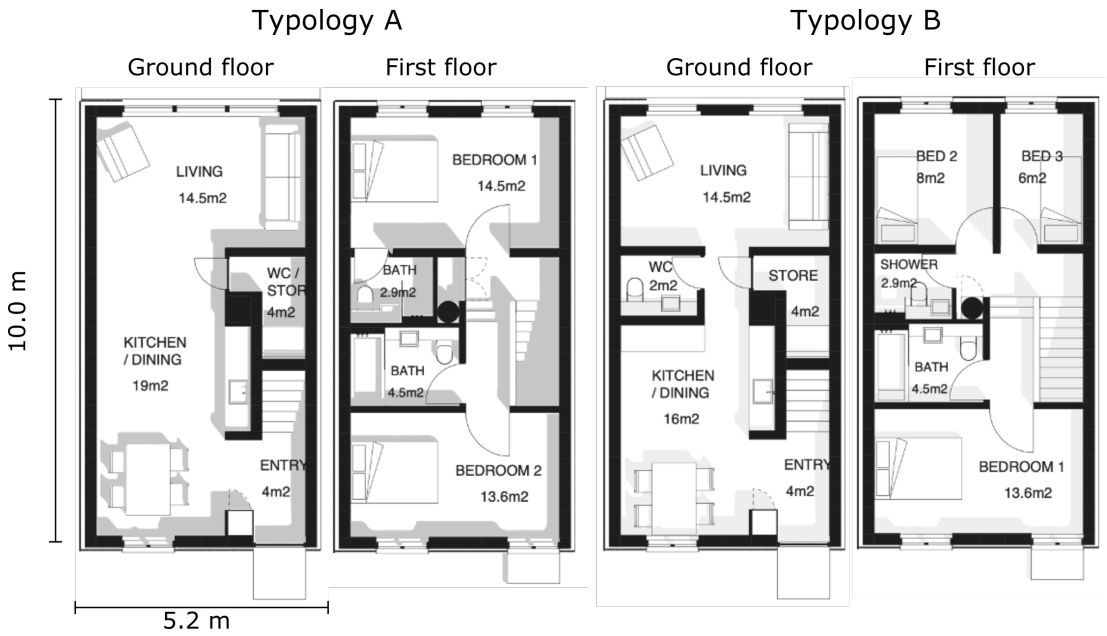


FIG. 3: Wikihouse Skylark possible architectural configurations.

In this framework, the digitally-fabricated, open-source building system *WikiHouse* (Figure 1) started development in 2014. WikiHouse consists of plywood hollow subassemblies (e.g. beams, columns, joints) manufactured by CNC machining plywood sheets, and assembled on site to build residential houses. The manufacturing process requires a 3-axis CNC machine, and the timber elements are cut out of 2.4 m $\times$ 1.2 m plywood panels. Such characteristics mean that WikiHouse can be repeatably produced at scale by a local network of small manufactures rather than large centralised facilities.

In 2020, a new WikiHouse system, *Skylark*, was developed (Figure 2) with the goal

of standardising the design, manufacturing, and assembly of building elements. This approach leads to a more efficient design and production, with consequent reduction in the cost and waste. The result is a library of common subassemblies that can be combined together to create a variety of architectural designs. In Figure 3, typical architectural layouts of a two storey WikiHouse are reported. Providing a functional and affordable housing unit where the internal architectural layout can be modified with some degree of flexibility was a key driver in developing the engineered structural system. Such layouts affected, among other variables, the suitable span lengths, beams and columns depths, and location of the shear walls.

The aim of this paper is to provide fundamental knowledge in terms of conceptual development, fabrication process and structural performance of Skylark. The structural performance was evaluated by means of experimental testing and analytical modelling. The main scope consists of the performance of the structural beams under gravity loads.

All Skylark 3D models, CNC cutting related files and assembly instructions are available under Creative Commons Share-alike licence at www.wikihouse.cc. The 3D models, CNC cutting files, and assembly instructions for the specimens tested are provided as supplemental material to this paper.

## DESCRIPTION OF THE SPECIMENS

The main gravity load resisting system transfers force through the beams and into the columns via the beam column joint. Columns are fixed to the foundation by conventional metal plate fasteners. Five beam specimens ( beams and mock columns ) were fabricated out of 2440 $\times$ 1220 $\times$ 18 mm plywood panels (Figure 4). The cutting was performed by a 3 axis CNC machine (Figure 4a), using an end mill compression cutter with diameter of 6.35 mm. Four plywood panels were used to make each beam specimen. The geometry of the specimens was optimized, among the other factors, to reduce the material waste to approximately 10%. The cutting time during prototyping for 1 beam specimen was between 140 minutes and 180 minutes. The moisture content of the timber was measured by an electrical resistance moisture meter to be in the range of 9.5% and 10.5%.

The timber panels were provided by Metsä, and the product is called ”Metsä Wood structural spruce plywood”. The mechanical properties of the plywood panels were tested by means of compression and tension tests according to BS EN 389:2004 (2005) and shear by direct shear tests on 38mm $\times$ 38mm $\times$ 18mm blocks. Results are summarized in Table 1.

Further details on the material testing are reported in Appendix A.

The assembly of the specimens consists of interlocking the timber panels with each other without the need for specialist equipment. The system relies on two main types of joint (Figure 5):

1. Stitched joints, which are used to create hollow box elements from the panels. Such joints connect panels with plane perpendicular to each other. These joints can be observed for example between the web and the flange in the beams and columns.


FIG. 4: Fabrication of the beams: a) CNC cutting, b) assembly of the mock columns and shear panel and c) assembly of the beams.

2. Castellated joints, which are used to create a longer element from to shorter ones. Such joints connect panels with plane parallel to each other. These joints can be observed for example in the flange and in the web of the beams.

Even if the main load transfer between the panels occurs via timber to timber contact, some 2 mm diameter nails were inserted to provide additional confining capacity. The assembly of the specimens was performed by a single operator, and the average time necessary to assemble one specimen was 15-20 minutes.

Beams (Figure 6 ) span over a length of 5155 mm (centre column to centre column), and have a overall section of 600 x 380 mm. Columns present a section equal to 600 x 316 mm. The shear panel allows to create continuity between column to column, and it will be activated in case of column or bream uplift. Note that the connection between

TABLE 1: Mechanical properties of plywood: $\sigma_c$ compression capacity, $E_c$ elastic modulus in compression, $\sigma_t$ tension capacity, $E_t$ elastic modulus in tension, $f_s$ shear capacity and $G$ shear modulus.

| | direction $\parallel$ | direction $\perp$ |
|---|---|---|
| $\sigma_c$ (MPa) | 24.6 | 15.4 |
| $E_c$ (MPa) | 9969 | 3549 |
| $\sigma_t$ (MPa) | 18.5 | 15.2 |
| $E_t$ (MPa) | 8532 | 4423 |
| $f_s$ (MPa) | 5.4 | *6.3 |
| $G$ (MPa) | 183.9 | *141.7 |

* No actual shear failure plane was identified.

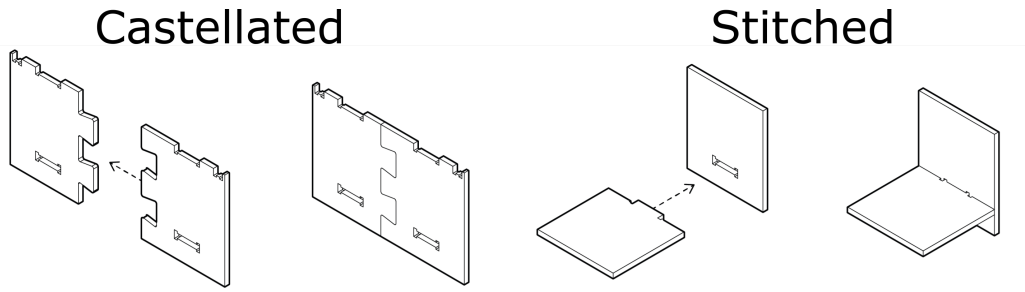


FIG. 5: Detailing of the castellated and stitched joints.

the beam and the column was developed with the aim of behaving like a pin, i.e., no bending moment transferred by the beam into the column. The purpose was to ensure the columns working primarily in compression and gravity loads.

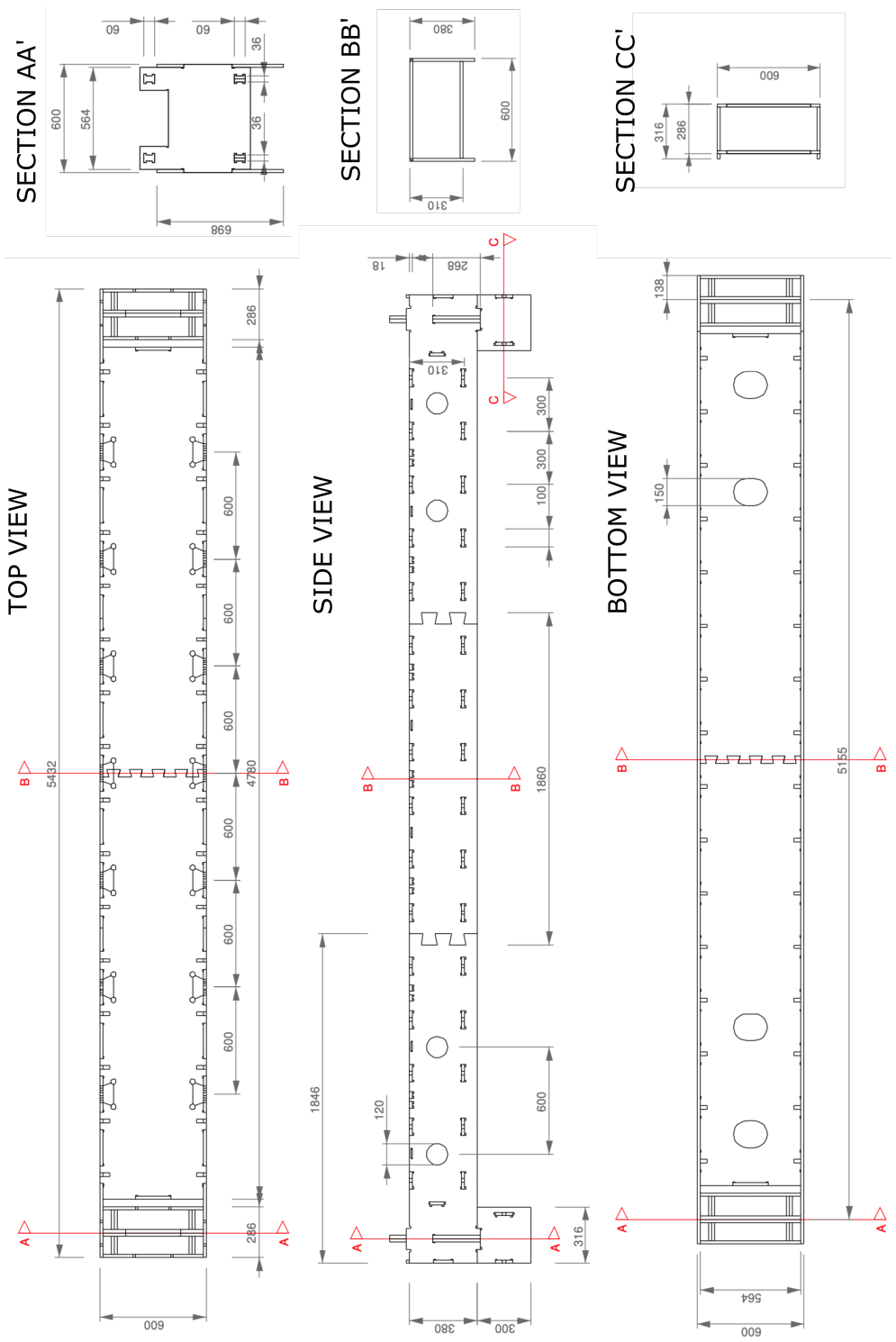


FIG. 6: Technical drawing of the beams.

## EXPERIMENTAL SETUP

The five beam specimens were tested in a 4-point bending test configuration (Figure 7) following the current standard of practice for I-timber beams ISO 22389-1 (2010). Since no specific standard covers the testing of hollow timber beams to the knowledge of the authors, ISO 22389-1 (2010) was chosen as the closest reference.

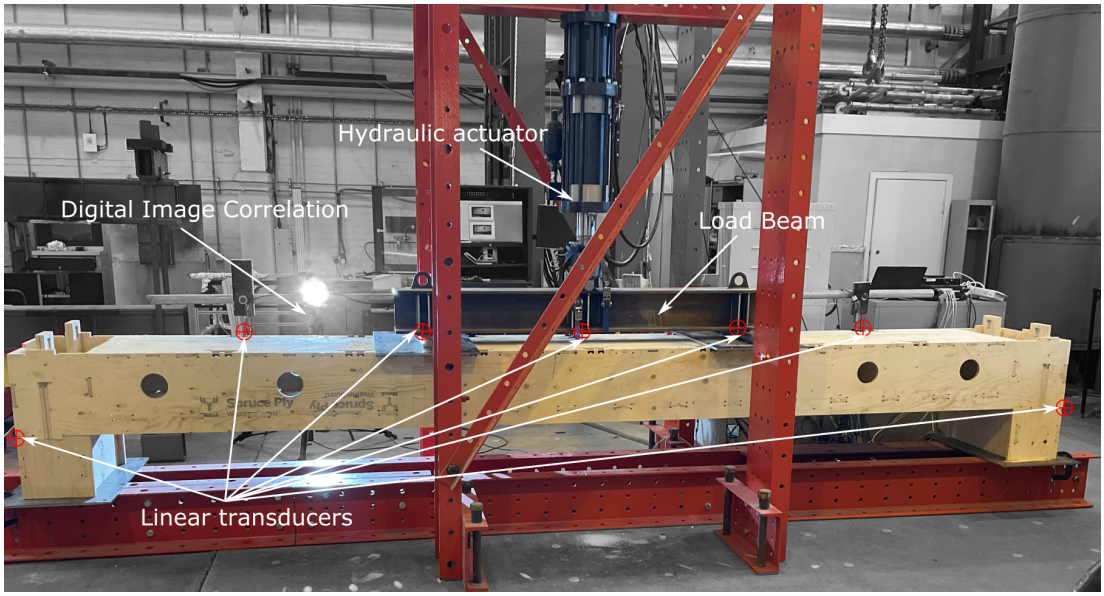


FIG. 7: Experimental setup for testing the specimens.

The load exerted by the hydraulic actuator was applied to the timber beams by using a 1.7 m long UC 203 x 203 x 71 mm steel profile and two 10 x 500 x 800 mm steel plates. Two 40 mm diameter steel bars were welded to the plates to create a pin connection between the load spreading beam and the timber specimens (Fig. 7). The plates were positioned so that the forces push on the timber specimen at 1.7 m and 3.4 m, i.e. approximately one third of the span measured from each column centre. The following instrumentation was installed for data acquisition:

1. 7 linear transducers were used to track the specimen displacement profile. Five of them were mounted to measure the beam's vertical deflection, while two of them were mounted to measure the gap opening between the beam and the column. The linear transducers on the beam were mounted in correspondence of L/4, L/3, L/2, 2L/3 and 3L/4 with L=5160 mm the beam span.
2. a 250 kN-capacity load cell was used to measure the actuator force.
3. a digital image correlation system was used to to track full-field displacement and strain on one side of the beam. Since the cameras' configuration geometry allows to focus on roughly 1.5 m length of the specimen, their position was changed between tests. They focused on the midspan section of the beam in the first 3 specimens, and on the castellated joint on the other two specimens.

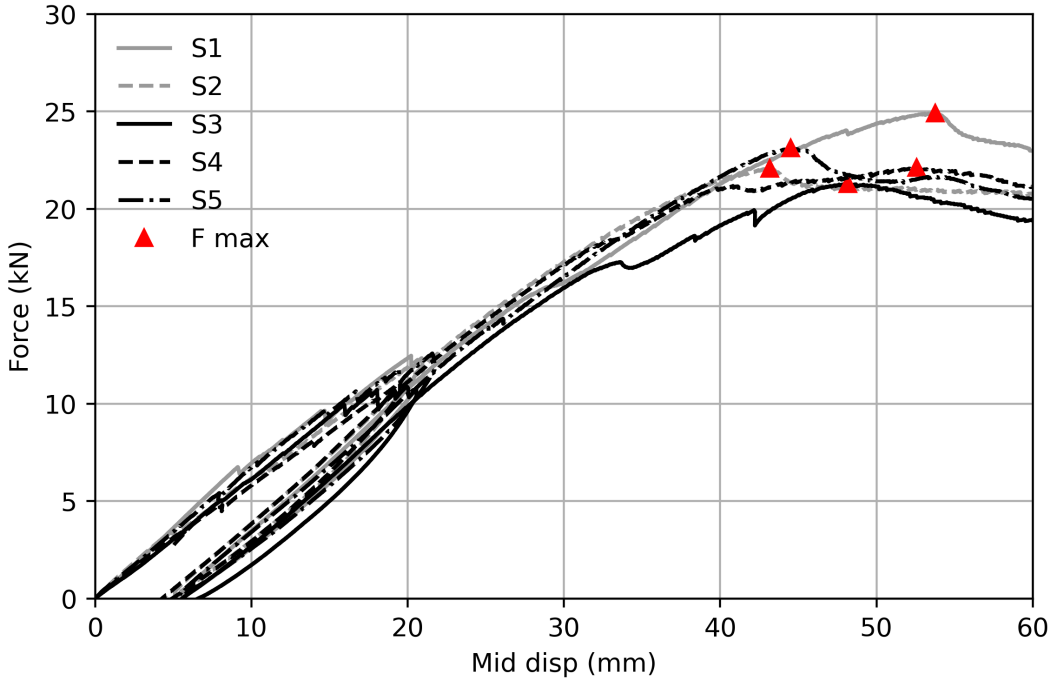


FIG. 8: Force-displacement curves for beam specimens.

The loading protocol approximately follows the guidance given in EN 1380:2009 (2009) for connectors in timber structures. Although the test is for a complete element rather than a connection, its behaviour is driven by local behaviour at connections between parts, and the cycle of loading recommended in that testing standard was used to capture the different stiffness of the system under initial loading, and the unload-reload cycle. The test was carried out in displacement control, with the actuator moving at 3 mm per minute. The loading protocol consisted a monotonic ramp of 22 mm (roughly span divided by 250), a one minute hold, a monotonic ramp back to 5 mm, a one minute hold, and then a monotonic ramp until failure.

## EXPERIMENTAL RESULTS

The response of the specimens in terms of force (exerted by the actuator) vs mid-span displacement is reported in Figure 8. The peak force was between 21.3 kN and 24.9 kN. Data are also reported in Table 2.

All specimens failed in a ductile manner: the specimens were able to maintain the load for a while after reaching the peak force. Such ductility was achieved because the failure occurred in the stitched joints, where local compressive failure occurred at the contact between the tab on the bottom flange and the web, as reported in Figure 9. In addition to the stitched joints, damage was also observed in the castellated joints, especially the joint placed at the bottom flange of the specimens.

It can be also observed in Fig. 9 that the joint panel opened a gap with the mock column, while no column uplift was identified during the test. This suggests the joint

TABLE 2: Experimental values: $F_{max}$; maximum force, $M_{max}$ maximum bending moment, $K_i$ initial elastic stiffness and $K_r$ reload elastic stiffness.

| **Specimen** | $F_{max}(kN)$ | $M_{max}(kNm)$ | $K_i(kN/m)$ | $K_r(kN/m)$ |
|---|---|---|---|---|
| S1 | 24.9 | 21.4 | 660 | 723 |
| S2 | 22.1 | 19.0 | 576 | 729 |
| S3 | 21.3 | 18.3 | 625 | 658 |
| S4 | 22.1 | 19.0 | 551 | 709 |
| S5 | 23.1 | 19.9 | 653 | 715 |

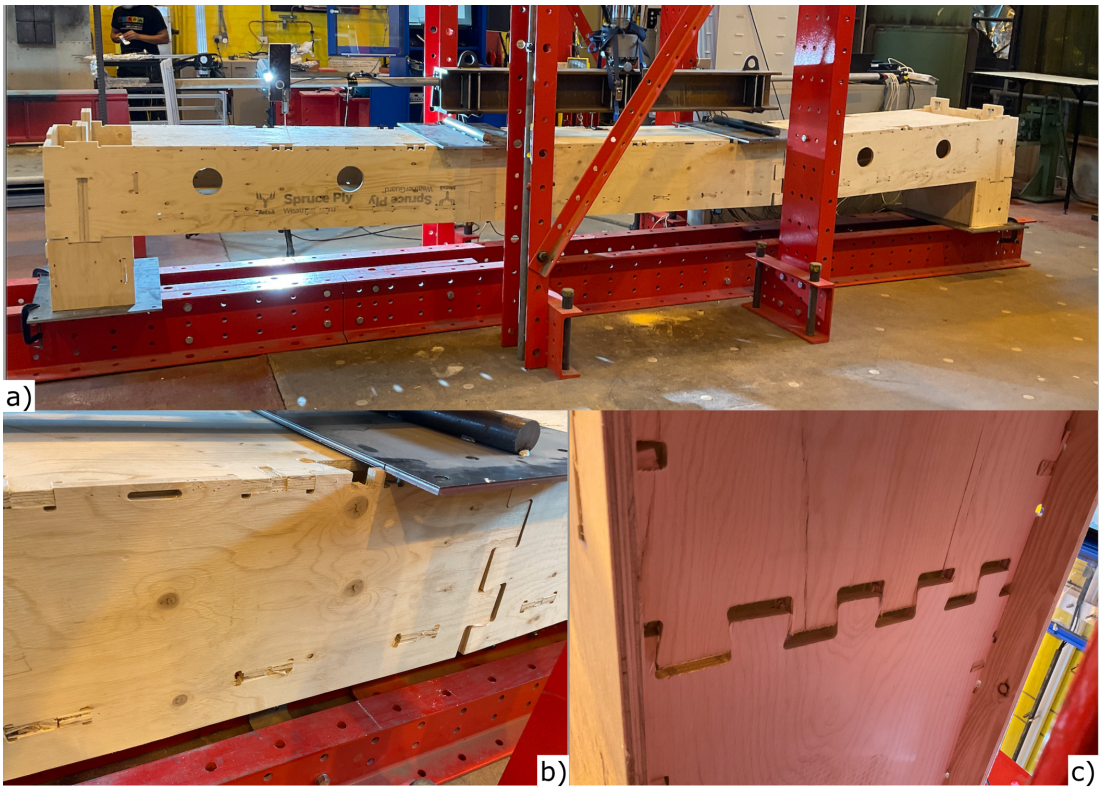


FIG. 9: Typical failure of the beam specimens: a) overview of the specimen at failure, b) detail of the stitched joints/ side dovetail joints. and c) detail of the bottom flange dovetail joint.

behaves as pin, i.e. only negligible (if any) amount of bending moment is transferred from the beam into the column. Considering a simply supported static scheme, the specimens showed a peak bending moment between 18.3 kNm and 21.4 kNm.

From Figure 8, it can be seen that the specimens do not follow the initial loading curve after they are unloaded. In other words, the specimens present a residual deformation when they are unloaded, which creates a shift in the re-loading branch with respect to the initial one. This is common in conventional timber connections with dowels or bolts which transfer load by contact over a small area as local plastic defor-

mation occurs even at low loads (Dorn et al. 2013; Reynolds et al. 2013). This effect is amplified in this system because of the several pegs in the stitched joints (Figure 5), which are manufactured to be 2 mm bigger than the holes. When inserted by hammer, they are subjected to an initial pre-compression. Hence they are more likely to sustain local plastic deformation at small loads. Such deformation is not recovered during unloading, and therefore a residual displacement exists.

The initial elastic stiffness of the specimens was calculated according to Eq. 1, based on EN 1380:2009 (2009):

$$K_i = \frac{F_{40\%} - F_{10\%}}{d_{40\%} - d_{10\%}} \tag{1}$$

where $F_{40\%}, F_{10\%}$ represent 40% and 10% of the maximum force (Fig. 8). Conversely, $d_{40\%}, d_{10\%}$ represent the displacement values where such force occurs. The elastic initial stiffness values $K_i$ are between 551 kN/m and 660 kN/m. The values for all the specimens are reported in Table 2. Similarly to what has been done for the initial beam stiffness $K_i$, a stiffness value $K_r$ corresponding to the reloading branch was also calculated. The value of $K_r$ ranged between 658 kN/m and 729 kN/m.

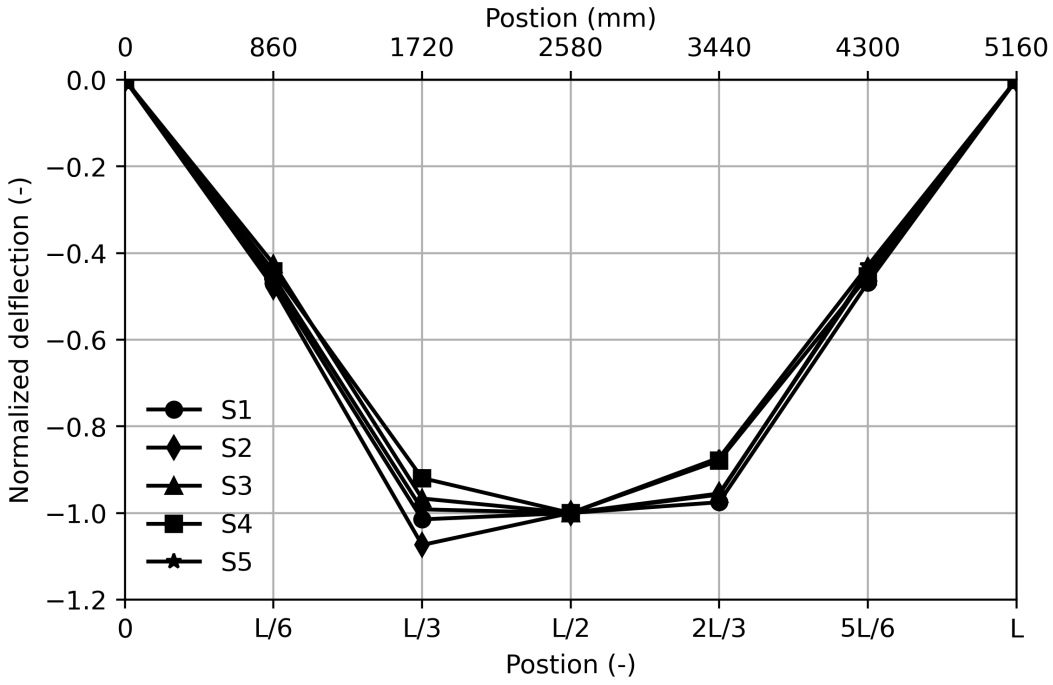


FIG. 10: Deflection profile of the specimens at 22mm.

The deflected shaped obtained from the linear transducers when the midspan of the specimens reached a typical SLS limit (22 mm or span / 250), is presented in Figure 10. These plots are normalised by the midspan deflection displacement for an easier comparison.

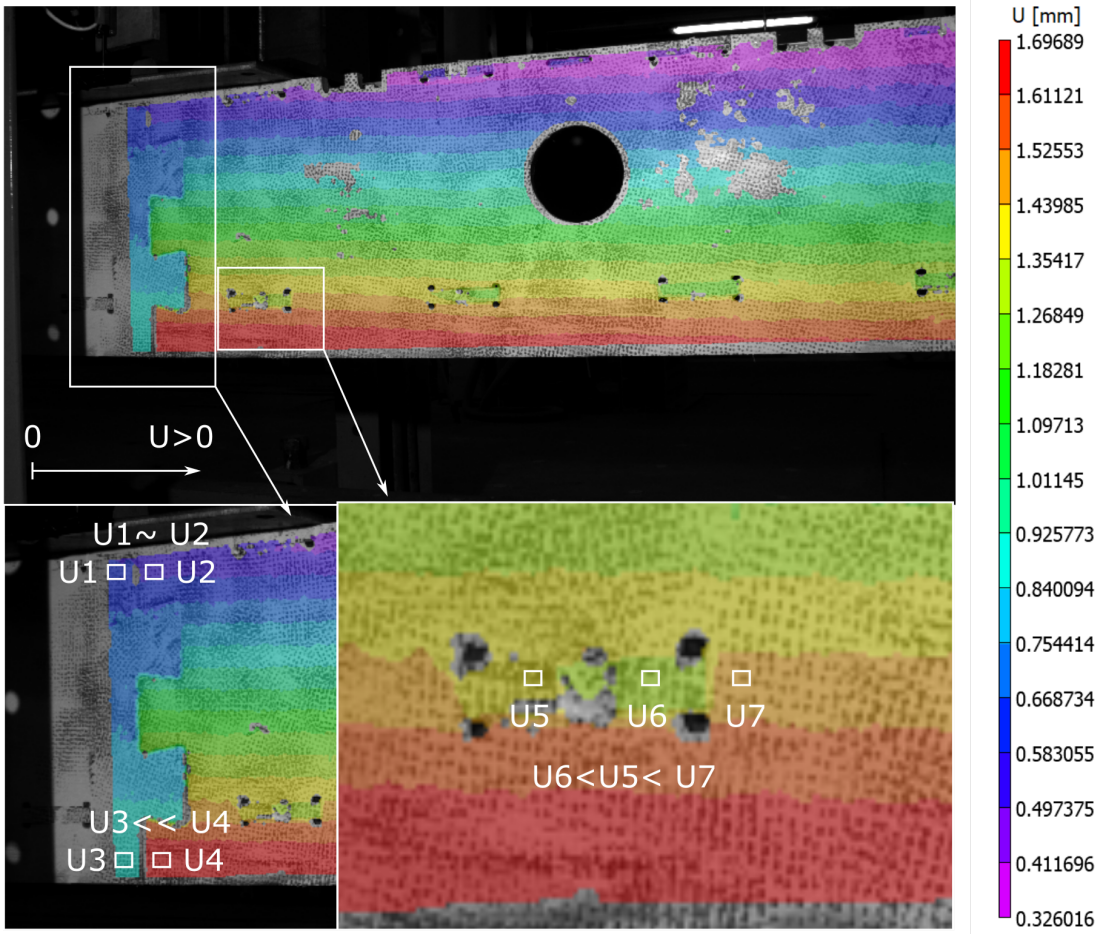


FIG. 11: Horizontal displacement measured on specimen 5 by using digital image correlation.

The displacement measurements in Figure 10 suggest that the beams do not deform according to Euler-Bernoulli's beam theory: that is, they do not bend as a monolithic beam would. Instead, a large proportion of their bending deflection comes from rotation at each of the castellated joints in the webs. This is caused by the gap opening in the castellated joint, which results in additional rigid-body rotation of the panels with respect to each other (Figure 10).

In Figure 11 the horizontal displacements measured by using DIC in specimen 5 show the rotation occurring in the castellated joint in the beam's web. It can be seen that, while at the top of the beam the horizontal displacement is similar across the joint, in the bottom part of the beam the displacement on the left side of the joint is different from the displacement of the right side of the joint. Thus the two parts of the web pivot about a point near the top of the beam.

The bottom right detail in Figure 11 shows the movement of the tab in the stitched joint relative to the timber of the web around it. The left side of the tab moves with and compresses the timber of the web. The right side of the tab moves away from the

timber around it, and there is some gap closing in the tab itself, around the central peg which was used to take up manufacturing tolerances. This shows the combined effect of the shear connection the tab provides to induce composite action in the beam, and its action holding together the lower part of the castellated joint in the web.

## ANALYTICAL MODEL

The behaviour of the specimens was modelled by considering a beam element with rotational springs at the castellated joints in the web (Figure 12).

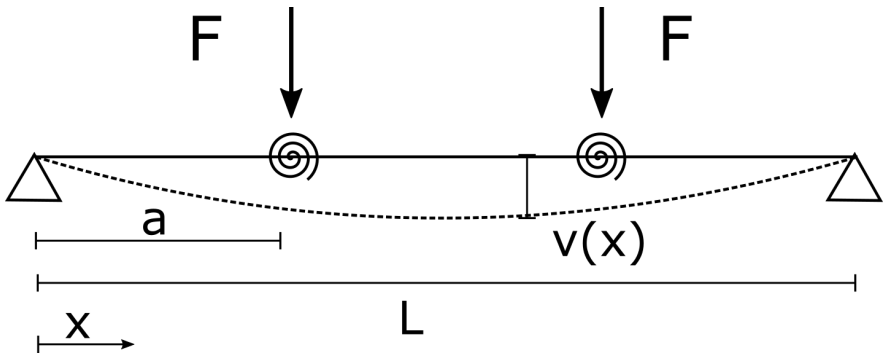


FIG. 12: Structural model of the beam.

The vertical displacement $v(x)$ of the beam can be calculated by using equation 2, which was derived by integrating Euler-Bernoulli equations (see Appendix B):

$$v(x) = \begin{cases} v^{left}(x) = -\frac{F}{6EI}x^3 + [-\frac{Fa^2}{2EI} + \frac{FaL}{2EI} + \frac{Fa}{k_r}]x & x \leq a \\ v^{right}(x) = -\frac{Fa}{2EI}x^2 + (\frac{FaL}{2EI})x + -\frac{Fa^3}{6EI} + \frac{Fa^2}{k_r} & a \leq x \leq 0.5L \end{cases} \tag{2}$$

with $E$ the elastic modulus, $I$ the inertia modulus, $a$ the distance of the castellated joint from the support, $L$ the span and $k_r$ the rotational stiffness of the joint.

The horizontal displacements across the castellated joint measured with DIC (Figure 13a) in specimen 5 were used to estimate the relative rotation. Specifically, the displacements in 6 points along the section depth were chosen to represent the section behaviour. The differential displacements across the castellated joint were then fitted with a linear function (Figure 13b) , so that the slope represents an estimate of the differential rotation.

The moment-rotation relationship of the joint is then reported in Figure 14. It can be noticed that the relationship appears to be linear until the moment reaches 7.5 kNm. The elastic initial rotational stiffness $k_r, i$, calculated between 10% and 40% of the peak value of the moment, is equal to 2295 kNm/rad. The unload-reload behaviour also follows a similar stiffness.

Equation 2 was the applied to estimate the beam deflection and compared with experimental results. Four cases where considered, i.e., when the midspan of the specimens reached 5 mm, 10 mm, 20 mm and 40 mm.

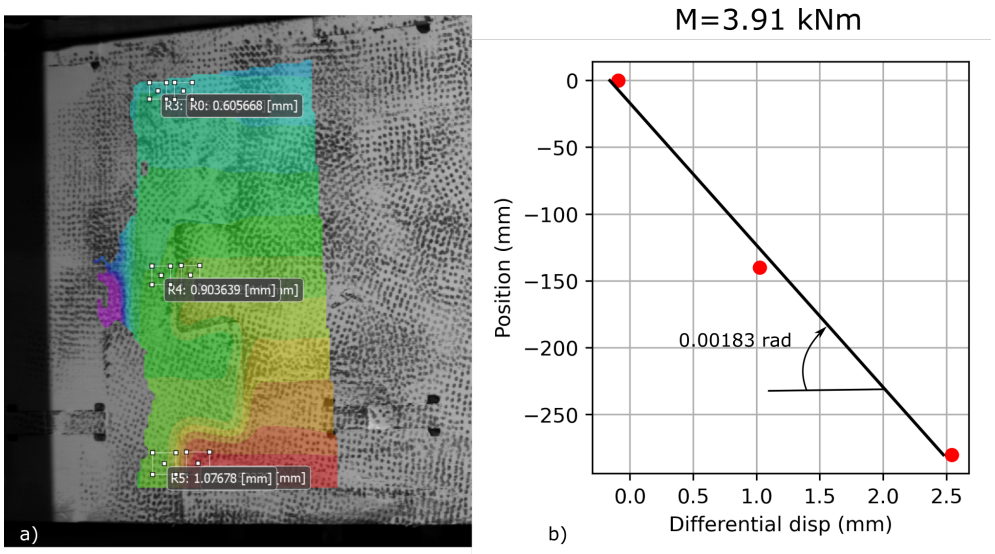


FIG. 13: a) extraction of the horizontal displacements in the representative points, and b) fitting of the differential displacements to estimate the relative rotation.

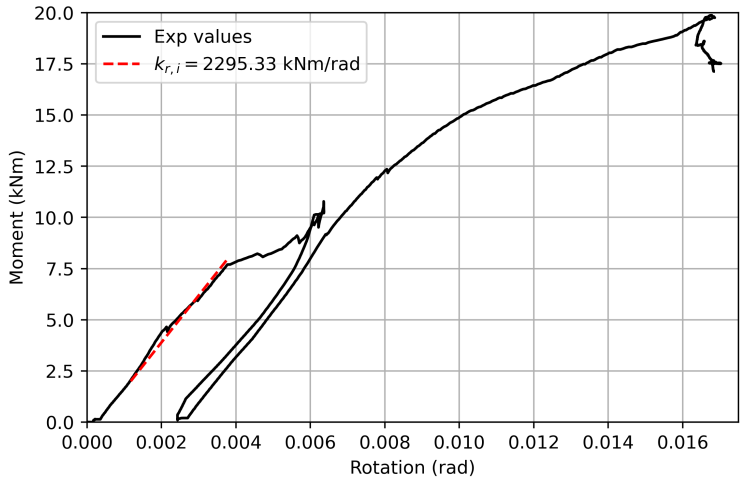


FIG. 14: Moment-rotation of the castellated joint.

The elastic modulus of the material $E$ was taken as 9251 MPa, which is the average between the elastic modulus in tension and the elastic modulus in compression (see Appendix A). The second moment of area of the section $I$ is equal to 523 $\times 10^6$ mm$^4$, and $k_r$ was taken as 2295 kNm/rad from Figure 14. The average force at the actuator corresponding to a midspan deflection of 5 mm, 10 mm, 20 mm and 40 mm is equal to 3.3 kN, 6.4 kN, 11.5 kN and 20.9 kN. These values can be derived from Figure 8. The deflected shape calculated by using the model is reported against the experimental results in Figure 15. For comparison, the deflected shape without the rotational springs

is also shown to illustrate the importance of the rotational flexibility of the castellated joint.

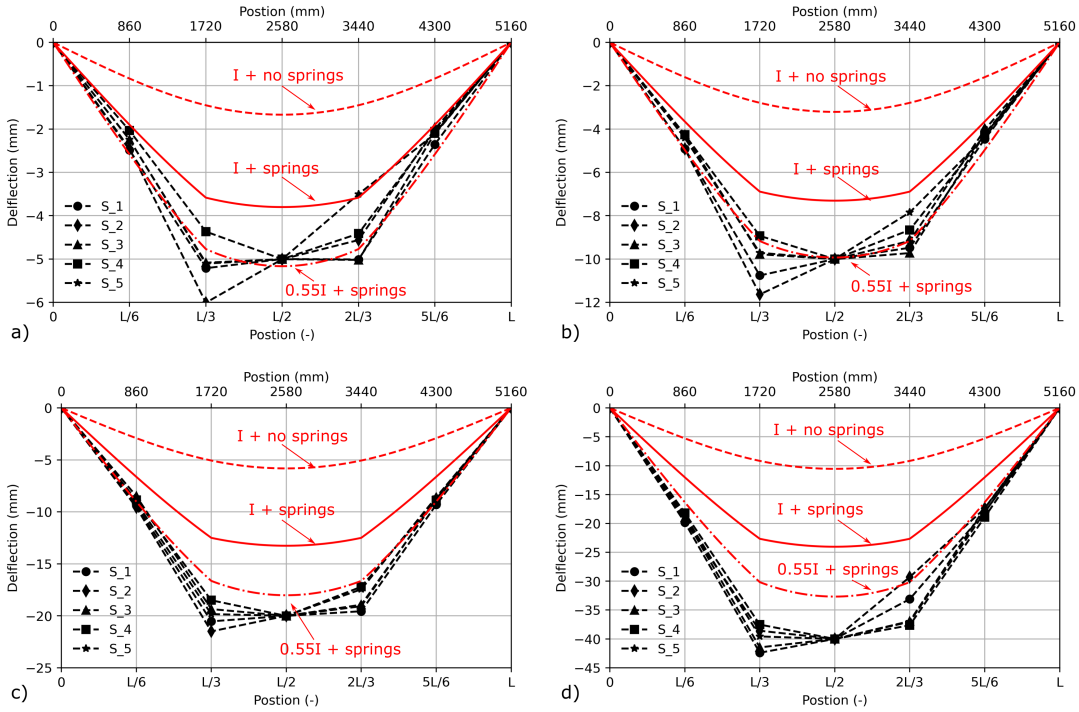


FIG. 15: Deflected shape: analytical model vs experimental results.

When the rotational springs are added, the analytical deflected shape better follows the experimental deflected shape. However, the model still underestimates the maximum deflection. This is due to the fact that the section was considered fully composite, i.e., the second moment of area $I$ was calculated considering full composite action between the different panels. In reality, there are relative displacements occurring between the panels due to construction tolerances and flexibility of joints. Such differential displacements will reduce the inertia of the whole section, which will increase the vertical deflection. As an example, a further deflected shape calculated by using 55% of the second moment of are $I$ is reported in Figure 15. It can be see that such deflection agrees much better with the experimental results, especially for mid-span deflection equal to 5 and 10 mm. For the higher deflections of 20 and 40 mm, plastic behaviour, probably in the stitched joints, is apparent, since the elastic model underestimates the deflections.

Figure 15 also shows that the model becomes less precise for increasing levels of vertical deflection. This occurs because the analytical solution is using a value of $k_r$ corresponding to the initial elastic branch of the moment-rotation diagram (Figure 14). However, for increasing levels of deflection, the relationship between rotation and moment becomes non-linear. Hence, $k_r$ decreases for higher rotations.

## CONCLUSION

A new system for constructing digitally fabricated timber houses, Wikihouse Skylark, was developed. Structural elements are CNC cut from 1.2 x 2.4 m plywood panels, and assembled into structural elements. Panels are connected together primarily by timber to timber joints. The gravity load-carrying capacity of the system was investigated by testing 5 full scale beam specimens in a 4 point bending test configuration. Furthermore, an analytical model considering rotational springs in correspondence of the castellated joint was developed, and compared against the experimental results. The main outcomes of the study can be summarized as:

1. All the beam specimens failed in a ductile manner, with the failing mechanisms due to the compression failure of the stitched joints, i.e., the joint between the beam bottom flange and the beam web.
2. No column uplift was observed during the test. This suggests that negligible bending moment (if any) is transferred into the columns.
3. The capacity of the beams was found between 18.3 kNm and 21.4 kNm. The average capacity was 19.5 kNm.
4. The castellated joint introduces extra flexibility to the beam element. The moment-rotation relationship of the joint is approximately linear up to a moment of 7.5 kNm. The initial rotational stiffness was estimated to be 2295 kNm/rad. If this flexibility is not taken into account, the deflection is significantly under-estimated.
5. The current analytical model, when the castellated joint flexibility is considered, agrees well with the experimental deflected shape in the initial elastic zone provided that the second moment of area of section is multiplied by 0.55. This coefficient is introduced to take into account the flexibility introduced by the stitched joints between the different panels.

Further specimens need to be tested for increasing the statistical significance of the results. Furthermore, further studies are necessary to determine the grade of composite action of the timber section out of the linear response to improve the accuracy of the analytical solution in outside of the linear domain.

The focus of the paper was placed on the concept, fabrication and structural performance of the paper. However, further research is also recommended to investigate the fire performance of the system.

## ACKNOWLEDGEMENTS

The authors would like to thank Paul Rutherford from Threecreate for manufacturing and assembling the timber specimens. The help of structural laboratory technicians at the University of Edinburgh Mark Partington, Jim Hutcheson and Calum Melrose is also greatly appreciated. The project was funded by Innovate UK, grant ID 77804.

## NOTATION

The following symbols are used in the paper:

$a$ = distance between the castellated joint and the support in the analytical model;
$A_c$ = cross sectional area of the specimen in the compression test;
$A_t$ = cross sectional area of the specimen in the tension test;
$A_s$ = cross sectional area of the specimen in the shear test;
$E$ = elastic modulus, average between tension and compression;
$E_c$ = elastic modulus in compression;
$E_t$ = elastic modulus in tension;
$F$ = force at the castellated joint in the analytical model;
$F_{max}$ = maximum force measured at the actuator;
$G$ = elastic shear modulus;
$I$= moudlus of inertia;
$k_r$ = rotational stiffness in the castellated joint;
$K_i$ initial elastic stiffness of the beams;
$K_r$ reload elastic stiffness of the beams;
$M$ = bending moment in the beams;
$PLY \updownarrow$ = refers to plywood specimens tested in the direction where 4 plies had the grain parallel to the load plane , and 2 plies had the grain perpendicular to the load plane;
$PLY \leftrightarrow$ = refers to plywood specimens tested in the direction where 4 plies had the grain perpendicular to the load plane , and 2 plies had the grain parallel to the load plane;
$d$ = vertical displacement measured during the material characterization tests;
$l_{e,i}$ = initial length of the extensometer in the material characterization tests;
$\sigma_c$ = compression stress in the compression test;
$\sigma_{c,m}$ = average compression strength;
$\sigma_t$ = tensile stress in the tensile test;
$\sigma_{t,m}$ = average tensile strength;
$\sigma_s$ = shear stress in the shear test;
$\sigma_{s,m}$ = average shear strength;
$\sigma_{40\%}, \sigma_{10\%}$ = value of stress corresponding to 40% and 10% of the peak stress;
$\varepsilon_c$ = compression strain in the compression test;
$\varepsilon_{40\%}, \varepsilon_{10\%}$ = value of strain corresponding to a stress equal to $\sigma_{40\%}$ and $\sigma_{10\%}$;

## REFERENCES


Arif, M., Goulding, J., and Rahimian, F. P. (2012). "Promoting off-site construction: Future challenges and opportunities." *Journal of Architectural Engineering*, 18(2), 75–78.

Beorkrem, C. (2017). *Material strategies in digital fabrication*. Routledge.

Boyd, N., Khalfan, M. M., and Maqsood, T. (2013). "Off-site construction of apartment buildings." *Journal of architectural engineering*, 19(1), 51–57.

CEN (2005). "BS EN 789:2004 Timber structures - Test methods -Determination of mechanical properties of wood based panels.

CEN (2009). "BS EN 1380:2009 Timber structures. Test methods. Load bearing nails, screws, dowels and bolts.

Dorn, M., de Borst, K., and Eberhardsteiner, J. (2013). "Experiments on dowel-type timber connections." *Engineering structures*, 47(0), 67–80.

Duncheva, T. and Bradley, F. F. (2019). "Multifaceted productivity comparison of off-site timber manufacturing strategies in mainland europe and the united kingdom." *Journal of Construction Engineering and Management*, 145(8), 04019043.

Gattas, J. and You, Z. (2016). "Design and digital fabrication of folded sandwich structures." *Automation in Construction*, 63, 79–87.

Goodier, C. I. and Gibb, A. G. F. (2005). "Barriers and opportunities for offsite in the uk." *Systematic Innovation in the Management of Project and Processes, Helsinki Int. Joint Symp.*, Helsinki, Finland: Technical Research Centre of Finland/Association of Finnish Civil Engineers, 148–158.

Hairstans, R. (2017). *Building offsite: An introduction*. Arcamedia Limited.

Hairstans, R. and Smith, R. E. (2018). "Offsite hub (scotland): establishing a collaborative regional framework for knowledge exchange in the uk." *Architectural Engineering and Design Management*, 14(1-2), 60–77.

Hosseini, M. R., Martek, I., Zavadskas, E. K., Aibinu, A. A., Arashpour, M., and Chileshe, N. (2018). "Critical evaluation of off-site construction research: A scientometric analysis." *Automation in Construction*, 87, 235–247.

International Organization for Standardization (2010). *ISO 22389-1:2010 Timber structures — Bending strength of I-beams — Part 1: Testing, evaluation and characterization*.

Krug, D. and Miles, J. (2013). "Offsite construction: Sustainability characteristics." *Buildoffsite: London, UK*.

Li, J.-M. and Knippers, J. (2015). "Segmental timber plate shell for the landesgartenschau exhibition hall in schwäbisch gmünd—the application of finger joints in plate structures." *International Journal of Space Structures*, 30(2), 123–139.

Magna, R. L., Gabler, M., Reichert, S., Schwinn, T., Waimer, F., Menges, A., and Knippers, J. (2013). "From nature to fabrication: biomimetic design principles for the production of complex spatial structures." *International Journal of Space Structures*, 28(1), 27–39.

Mayo, J. (2015). *Solid wood: case studies in mass timber architecture, technology and design*. Routledge.

Nguyen, A. C., Vestartas, P., and Weinand, Y. (2019). "Design framework for the struc-

tural analysis of free-form timber plate structures using wood-wood connections." *Automation in Construction*, 107, 102948.

Nguyen, A. C. and Weinand, Y. (2018). "Development of a spring model for the structural analysis of a double-layered timber plate structure with through-tenon joints." *World Conference of Timber Engineering 2018*, number CONF, World Conference of Timber Engineering.

Pan, W., Gibb, A. G., and Dainty, A. R. (2008). "Leading uk housebuilders' utilization of offsite construction methods." *Building Research & Information*, 36(1), 56–67.

Pan, W. and Sidwell, R. (2011). "Demystifying the cost barriers to offsite construction in the uk." *Construction Management and Economics*, 29(11), 1081–1099.

Rad, A. R., Weinand, Y., and Burton, H. (2019). "Experimental push-out investigation on the in-plane force-deformation behavior of integrally-attached timber through-tenon joints." *Construction and Building Materials*, 215, 925–940.

Reynolds, T., Harris, R., and Chang, W.-S. (2013). "Viscoelastic embedment behaviour of dowels and screws in timber under in-service vibration." *European Journal of Wood and Wood Products*, 71(5), 623–634.

Robeller, C. (2015). "Integral mechanical attachment for timber folded plate structures." *Report no.*, EPFL.

Robeller, C., Gamerro, J., and Weinand, Y. (2017). "Théâtre vidy lausanne–a double-layered timber folded plate structure." *Journal of the International Association for Shell and Spatial Structures*, 58(4), 295–314.

Sass, L. (2007). "Synthesis of design production with integrated digital fabrication." *Automation in construction*, 16(3), 298–310.

Sass, L. and Botha, M. (2006). "The instant house: a model of design production with digital fabrication." *International Journal of Architectural Computing*, 4(4), 109–123.

Stitic, A., Nguyen, A. C., Rezaei Rad, A., and Weinand, Y. (2019). "Numerical simulation of the semi-rigid behaviour of integrally attached timber folded surface structures." *Buildings*, 9(2), 55.

Švajlenka, J. and Kozlovská, M. (2020). "Evaluation of the efficiency and sustainability of timber-based construction." *Journal of Cleaner Production*, 259, 120835.

Willmann, J., Knauss, M., Bonwetsch, T., Apolinarska, A. A., Gramazio, F., and Kohler, M. (2016). "Robotic timber construction—expanding additive fabrication to new dimensions." *Automation in construction*, 61, 16–23.

## APPENDIX A: MATERIAL CHARACTERIZATION

The results of the material characterization in tension, compression and shear are below reported. The plywood used is made up of spruce, and uses 4 x 3 mm plies with grain parallel to the panel longer direction, and 2 x 3 mm plies with grain parallel to the panel shorter direction (Figure 16). At the time of testing, specimens had moisture content between 9.5% and 10.5%, which was measured by means of a moisture meter.

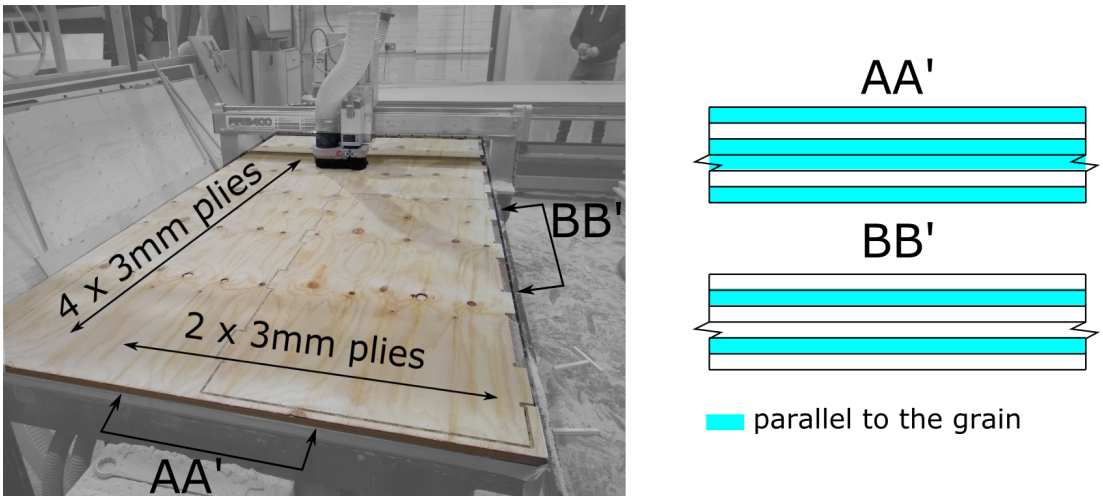


FIG. 16: Orientation of the plies in the panel.

### Compression

To evaluate the compression properties of plywood, 10 specimens were tested on a universal testing machine (Figure 17) according to the BS EN 789 (2005). Specimens are made of three 18 x 67 x 300 mm blocks tested together, and specifically:

1. 5 plywood specimens were tested in the direction where 4 plies had the grain parallel to the load direction, and 2 plies had the grain perpendicular to the load direction (labelled $PLY \updownarrow$).
2. 5 plywood specimens were tested in the direction where 2 plies had the grain parallel to the load direction, and 4 plies had the grain perpendicular to the load direction (labelled $PLY \leftrightarrow$),.

Load and displacement were monitored by using a load cell of the universal testing machine and an extensometer installed on the specimen, respectively. Compression stress $\sigma_c$ and compression strain $\varepsilon_c$ were calculated by using equation 3:

$$\sigma_c = \frac{F}{A_c} \qquad \varepsilon_c = \frac{d}{l_{e,i}} \tag{3}$$

where $F$ the vertical force exerted by the actuator, $A_c = 3618mm^2$ the cross section area of the specimen, $d$ the vertical displacement measured by the extensometer, and $l_{e,i}$ the initial length of the extensometer.

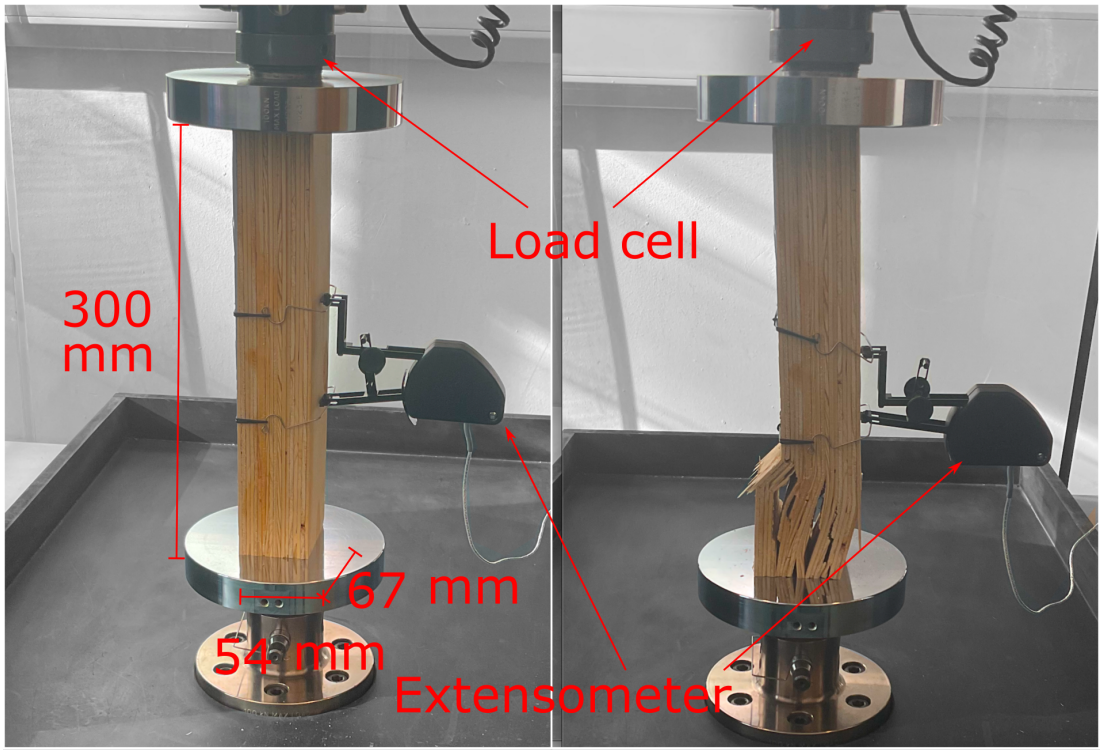


FIG. 17: Standard compression test.

Stress-strain curves are shown in Figure 18, while the most relevant quantities, including average compression strength $\sigma_{c,m}$ and average elastic compression modulus $E_c$ are reported in Table 3. $E_c$ was calculated according to equation 4:

$$E_c = \frac{\sigma_{40\%} - \sigma_{10\%}}{\varepsilon_{40\%} - \varepsilon_{10\%}} \tag{4}$$

where $\sigma_{40\%}, \sigma_{10\%}$ represent 40% and 10% of the compression maximum stress, respectively (Fig. 18). $\varepsilon_{40\%}, \varepsilon_{10\%}$ are the values of strain where such compression stress occurs.

From Fig. 18 and Table 3, it can be noticed that:

1. $PLY \updownarrow$ shows an average compression strength equal to 24.6 MPa, and an elastic compression modulus equal to 9969 MPa.
2. $PLY \leftrightarrow$ shows an average compression strength equal to 15.4 MPa, and an elastic compression modulus equal to 3549 MPa.

**Tension**

To evaluate the tensile properties of plywood, 10 specimens were tested on a universal testing machine (Figure 19) according to the BS EN 789 (2005). Specimens are 1 m long, 18 mm thick, 250 mm wide at the end section, and 150 mm wide at the middle section as per BS EN 789 (2005). A bolted connection was designed to allow

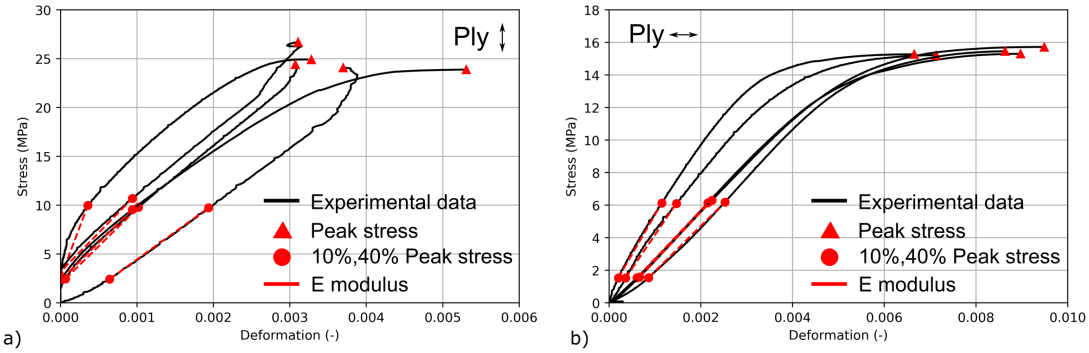


FIG. 18: Compression test results.

TABLE 3: Compression test results: $\sigma_{max}$ peaks compression stress; $\varepsilon_{10\%}$, $\varepsilon_{40\%}$ deformation at 10% and 40% of the peak stress, respectively; $E_c$ elastic compression modulus.

| **Material** | **Specimen** | $\varepsilon_{10\%}$ **(-)** | $\varepsilon_{40\%}$ **(-)** | $\sigma_{c,max}$ **(Mpa)** | $E_c$ **(Mpa)** |
|---|---|---|---|---|---|
| $PLY \updownarrow$ | 1 | -1.39e-06 | 0.000357 | 24.9 | 20806 |
| | 2 | 6.58e-05 | 0.00102 | 24.4 | 7692 |
| | 3 | 1.22e-05 | 0.000939 | 23.9 | 7719 |
| | 4 | -5.58e-05 | 0.000941 | 26.7 | 7984 |
| | 5 | 0.000643 | 0.00194 | 24.1 | 5645 |
| | | | | 24.6 | 9969 |
| $PLY \leftrightarrow$ | 1 | 0.000609 | 0.00215 | 15.3 | 2979 |
| | 2 | 0.000363 | 0.00147 | 15.2 | 4144 |
| | 3 | 0.000665 | 0.00225 | 15.7 | 2983 |
| | 4 | 0.000203 | 0.00115 | 15.3 | 4854 |
| | 5 | 0.000862 | 0.00253 | 15.5 | 2786 |
| | | | | 15.4 | 3549 |

the force transfer from the universal testing machine into the specimen (Figure 19. In order to ensure the failure occurring on the specimen reduced section and not in the bolted connection, two 9 x 300 X 180 mm plywood panels were glued on both ends of the specimens. Specifically, the following specimens were tested:

1. 5 plywood specimens were tested in the direction where 4 plies had the grain parallel to load direction , and 2 plies had the grain perpendicular to the load direction (labelled $PLY \updownarrow$).
2. 5 plywood specimens were tested in the direction where 2 plies had the grain

perpendicular to the load direction, and 4 plies had the grain parallel to the load direction (labelled $PLY \leftrightarrow$).

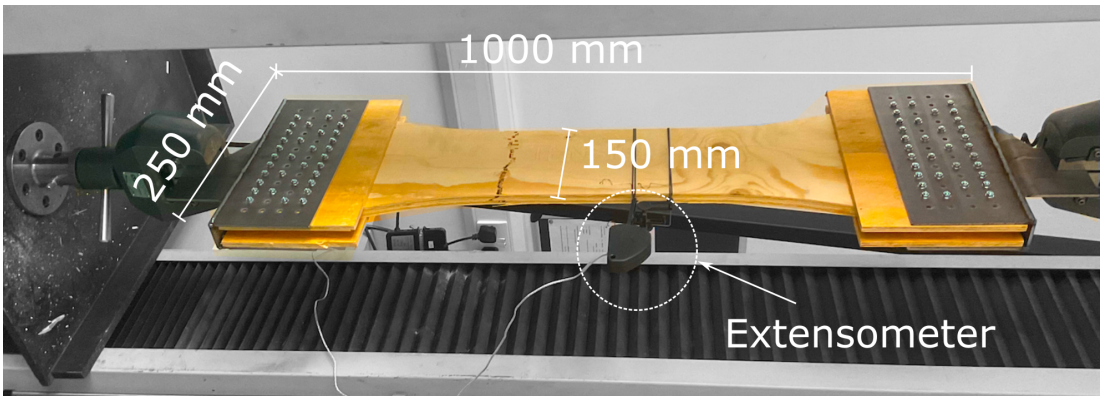


FIG. 19: Standard tensile test.

Load and displacement were monitored by using a load cell of the universal testing machine and an extensometer installed on the specimen, respectively. Tensile stress $\sigma_t$ and tensile strain $\varepsilon_t$ were calculated by using equation 5:

$$\sigma_t = \frac{F}{A_t} \qquad \varepsilon_c = \frac{d}{l_{e,i}} \tag{5}$$

where $F$ the vertical force exerted by the actuator, $A_t = 2700mm^2$ the mid-span cross section of the specimen, $d$ the vertical displacement measured by the extensometer, and $l_{e,i}mm$ the initial length of the extensometer.

Stress-strain curves are shown in Figure 20, while the most relevant quantities, including average tensile strength $\sigma_{t,m}$ and average tensile modulus $E_m$, are reported in Table 4. $E_m$ was calculated according to equation 6:

$$E_m = \frac{\sigma_{40\%} - \sigma_{10\%}}{\varepsilon_{40\%} - \varepsilon_{10\%}} \tag{6}$$

where $\sigma_{40\%}, \sigma_{10\%}$ represent 40% and 10% of the tensile maximum stress, respectively (Fig. 20). $\varepsilon_{40\%}, \varepsilon_{10\%}$ are the values of strain where such tensile stress occurs.

From Fig. 20 and Table 4, it can be noticed that:

1. $PLY \updownarrow$ shows an average tensile strength equal to 18.5 MPa, and an elastic tension modulus equal to 8532 MPa.
2. $PLY \leftrightarrow$ shows an average tension strength equal to 15.2 MPa, and an elastic tension modulus equal to 4423 MPa.

**Shear**

To evaluate the shear properties of plywood, 16 specimens were tested on a shear apparatus (Figure 21). It was decided to test more specimens in shear with respect

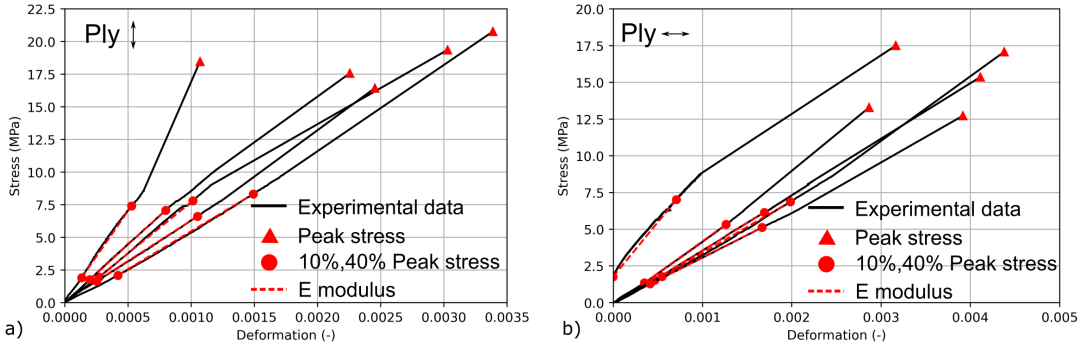


FIG. 20: Tensile test results.

TABLE 4: Tensile test results: $\sigma_{max}$ peaks tensile stress; $\varepsilon_{10\%}$, $\varepsilon_{40\%}$ deformation at 10% and 40% of the peak stress, respectively; $E_t$ elastic tension modulus.

| **Material** | **Specimen** | $\varepsilon_{10\%}$ **(-)** | $\varepsilon_{40\%}$ **(-)** | $\sigma_{max}$ **(Mpa)** | $E_t$ **(Mpa)** |
|---|---|---|---|---|---|
| $PLY$ ↕ | 1 | 0.000419 | 0.00149 | 20.8 | 5804 |
| | 2 | 0.000270 | 0.00101 | 19.4 | 7860 |
| | 3 | 0.000252 | 0.00105 | 16.4 | 6211 |
| | 4 | 0.000133 | 0.000527 | 18.5 | 13936 |
| | 5 | 0.000197 | 0.000798 | 17.6 | 8849 |
| | | | | 18.5 | 8532 |
| $PLY$ ↔ | 1 | 0.000348 | 0.00126 | 13.3 | 4353 |
| | 2 | 0.000464 | 0.00169 | 15.4 | 3743 |
| | 3 | 0.000545 | 0.00198 | 17.1 | 3544 |
| | 4 | 0.000413 | 0.00167 | 12.7 | 3064 |
| | 5 | -3.52e-06 | 0.000706 | 17.5 | 7412 |
| | | | | 15.2 | 4423 |

to compression and tension because higher variability was expected. Specimens are made of two 38 x 38 x 18 mm blocks tested together, and specifically:

1. 8 plywood specimens were tested in the direction where 4 plies had the grain parallel to the shear plane , and 2 plies had the grain perpendicular to the shear plane (labelled $PLY$ ↕).
2. 8 plywood specimens were tested in the direction where 2 plies had the grain parallel to the shear plane, and 4 plies had the grain perpendicular to the shear plane (labelled $PLY$ ↔),.

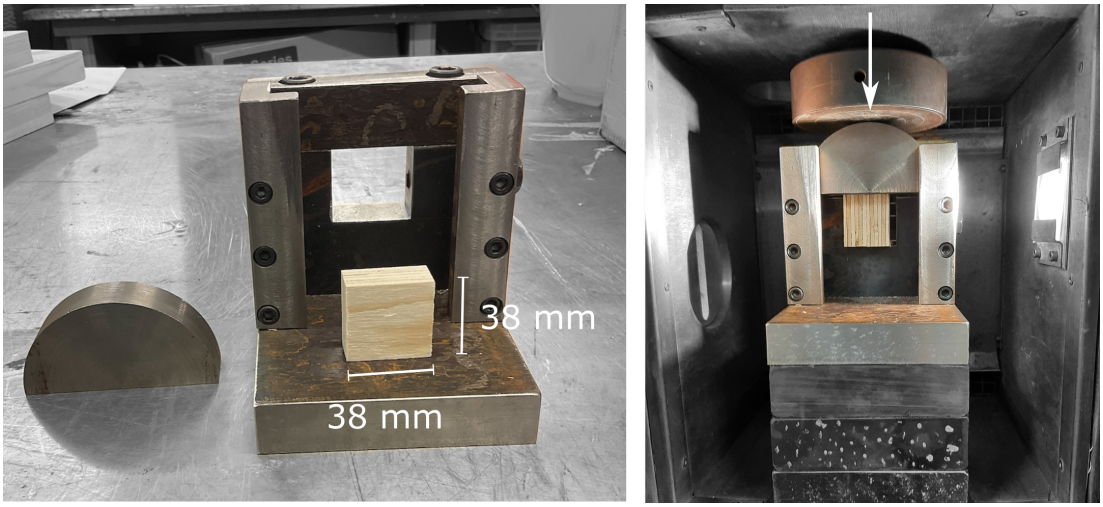


FIG. 21: Shear apparatus.

Load and displacement were monitored by using a load cell and and the loading head displacement of the universal testing machine. Shear stress $\sigma_s$ and shear strain $\varepsilon_s$ were calculated by using equation 7:

$$\sigma_s = \frac{F}{A_s} \qquad \varepsilon_s = \frac{d}{l_s} \tag{7}$$

where $F$ the vertical force exerted by the actuator, $A_s = 1444mm^2$ the shear area of the specimen, $d$ the vertical displacement and $l_s = 38mm$ the length of the specimen.

In Figure 22, the typical failure modes of the specimens are reported. $PLY \updownarrow$ shows a true shear failure: the shear plane in in fact clearly visible, and the wood fibers displace relative to each other. $PLY \leftrightarrow$ show more a local crushing rather than a failure along a shear plane.

Stress-strain curves are shown in Figure 23, while the most relevant quantities, including average shear strength $f_{s,m}$ and average shear modulus $G_m$ are reported in Table 5. $G_m$ was calculated according to equation 8:

$$G_m = \frac{\sigma_{40\%} - \sigma_{10\%}}{\varepsilon_{40\%} - \varepsilon_{10\%}} \tag{8}$$

where $\sigma_{40\%}, \sigma_{10\%}$ represent 40% and 10% of the shear maximum stress, respectively (Fig. 23). $\varepsilon_{40\%}, \varepsilon_{10\%}$ are the values of strain where such shear stress occurs.

From Fig. 23 and Table 5, it can be noticed that:

1. $PLY \updownarrow$ shows an average shear strength equal to 5.4 MPa, and an average shear modulus equal to 183.9 MPa.
2. $PLY \leftrightarrow$ shows an average shear strength equal to 15.2 MPa, and a shear modulus equal to 141.7 MPa.

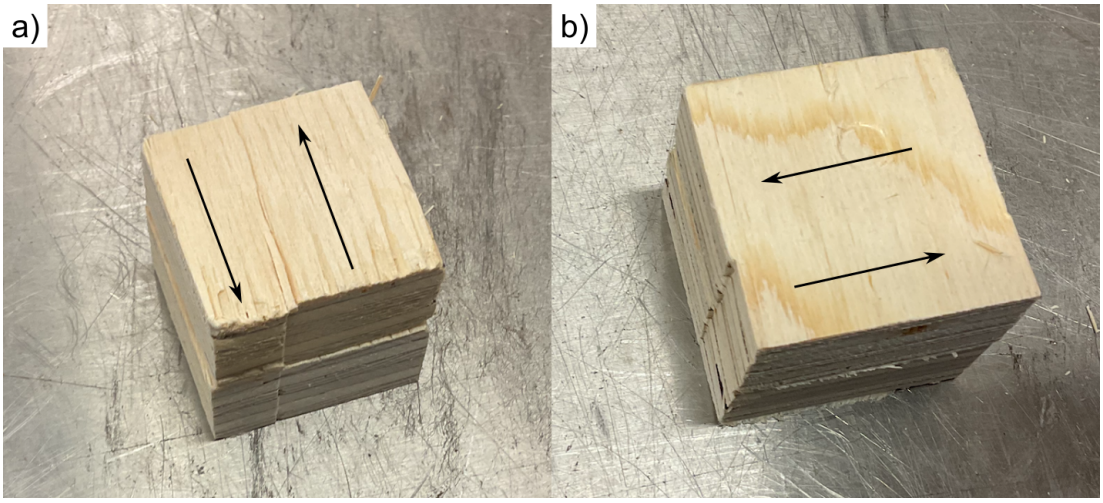


FIG. 22: Typical failures observed in the specimens: a)$PLY \updownarrow$, b) $PLY \leftrightarrow$.

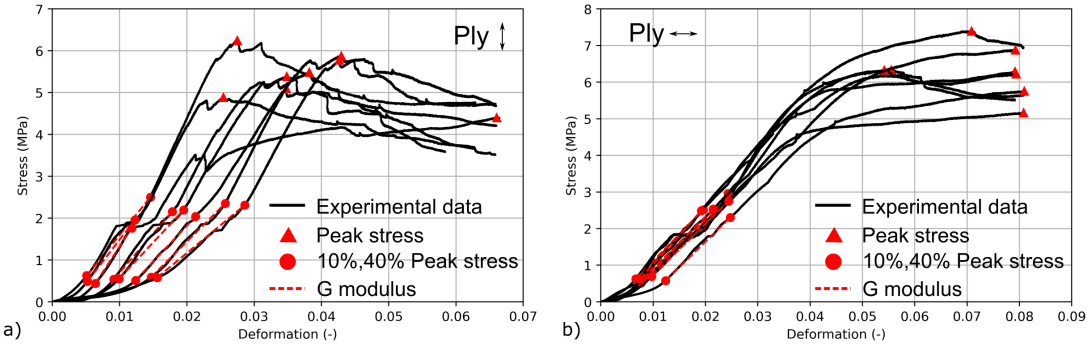


FIG. 23: Stress-strain curves for the each of the tested specimens.

## APPENDIX B: DERIVATION OF THE DEFORMED SHAPE

According to Euler-Bernoulli equations, the vertical deflection $v(x)$ and rotation $\phi(x)$ of the beam can be written a as:

$$\frac{\mathrm{d}^2 v(x)}{\mathrm{d}x^2} = \frac{\mathrm{d}\phi(x)}{\mathrm{d}x} = \frac{-M(x)}{EI} \tag{9}$$

where $E$ the elastic modulus, $I$ the modulus of inertia and $M(x)$ the bending moment function of the position coordinate $x$ (Figure 24).

The bending moment $M(x)$ is expressed by equation 10:

$$M(x) = \begin{cases} Fx & x \leq a \\ Fa & a \leq x \leq 0.5L \end{cases} \tag{10}$$

with $a$ the distance between the point of load application and the support, and $L$ the span. Note that the deflection is symmetric, therefore the problem is studied for $0 \leq x \leq 0.5L$.

TABLE 5: Shear test results: $\sigma_{max}$ peaks shear stress; $\varepsilon_{10\%}$, $\varepsilon_{40\%}$ deformation at 10% and 40% of the peak stress, respectively; $G_s$ shear modulus.

| **Material** | **Specimen** | $\varepsilon_{10\%}$ **(-)** | $\varepsilon_{40\%}$ **(-)** | $\sigma_{max}$ **(MPa)** | $G_s$ **(MPa)** |
|---|---|---|---|---|---|
| | 1 | 0.0051 | 0.0146 | 6.24 | 197.0 |
| | 2 | 0.0091 | 0.0178 | 5.39 | 186.3 |
| | 3 | 0.0064 | 0.0118 | 4.40 | 243.9 |
| | 4 | 0.0124 | 0.0213 | 5.10 | 171.4 |
| $PLY \updownarrow$ | 5 | 0.0147 | 0.0257 | 5.87 | 160.3 |
| | 6 | 0.0156 | 0.0286 | 5.78 | 133.0 |
| | 7 | 0.0099 | 0.0195 | 5.48 | 171.3 |
| | 8 | 0.0052 | 0.0123 | 4.88 | 207.8 |
| | | | | 5.4 | 183.9 |
| | 1 | 0.0077 | 0.0198 | 5.16 | 127.5 |
| | 2 | 0.0078 | 0.0223 | 6.33 | 130.7 |
| | 3 | 0.0094 | 0.0243 | 7.39 | 149.0 |
| | 4 | 0.0124 | 0.0247 | 5.75 | 139.7 |
| $PLY \leftrightarrow$ | 5 | 0.0080 | 0.0214 | 6.32 | 141.3 |
| | 6 | 0.0067 | 0.0196 | 6.29 | 146.1 |
| | 7 | 0.0074 | 0.0192 | 6.22 | 158.6 |
| | 8 | 0.0097 | 0.0244 | 6.88 | 140.2 |
| | | | | 6.3 | 141.7 |

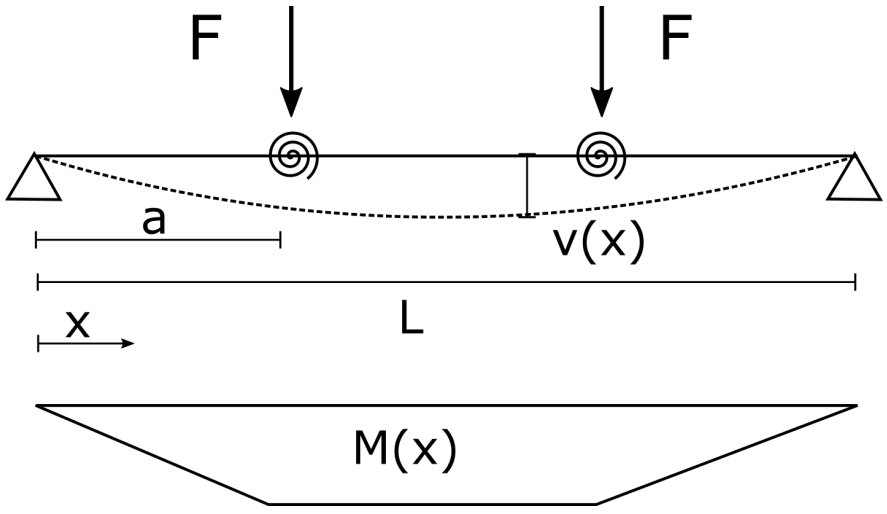


FIG. 24: Representation of the structural model and bending moment function.

Integrating equation 9 and substituting the bending moment function expressed by equation 10 leads to new expression for rotation $\phi(x)$ and vertical deflection $v(x)$,

which are presented in equation 11 and equation 12:

$$\phi(x) = \begin{cases} \phi^{left}(x) = -\frac{F}{2EI}x^2 + C_1 & x \leq a \\ \phi^{right}(x) = -\frac{Fa}{EI}x + D_1 & a \leq x \leq 0.5L \end{cases} \tag{11}$$

$$v(x) = \begin{cases} v^{left}(x) = -\frac{F}{6EI}x^3 + C_1 x + C_2 & x \leq a \\ v^{right}(x) = -\frac{Fa}{2EI}x^2 + D_1 x + D_2 & a \leq x \leq 0.5L \end{cases} \tag{12}$$

with $C_1, C_2, D_1, D_2$ constants of integration. These last be determined by considering the boundary conditions according to equation 13:

$$\begin{cases} v_{(x=0)} = 0 \\ \phi_{(x=0.5L)} = 0 \\ \phi^{left}_{(x=a)} - \phi^{righ}_{(x=a)} = \frac{M_{(x=a)}}{k_r} \\ v^{left}_{(x=a)} = v^{righ}_{(x=a)} \end{cases} \tag{13}$$

with $k_r$ the rotational stiffness of the spring. The boundary conditions express that:

1. the vertical displacement at the support is equal to 0 (because of the support).
2. the rotation in the midspan is equal to 0 (because of the symmetry of the deflected shape).
3. the difference of rotation in correspondence of the rotational spring is proportional to the moment and the spring stiffness.
4. there is no differential vertical displacement in correspondence of the spring (continuity of the element).

Solving the system of equations 13, 11 and 12 allows to determine the following values for the constants of integration:

$$\begin{cases} C_1 = -\frac{Fa^2}{2EI} + \frac{FaL}{2EI} + \frac{Fa}{k_r} \\ C_2 = 0 \\ D_1 = \frac{FaL}{2EI} \\ D_2 = -\frac{Fa^3}{6EI} + \frac{Fa^2}{k_r} \end{cases} \tag{14}$$

Note that the same results could be obtained by alternative integration methods, such as for example the Macaulay's method.